# Microstructure and Properties of NbVZr Refractory Complex

## **Concentrated Alloys**

- 3 Mu Li<sup>a</sup>, Zhaohan Zhang<sup>b</sup>, Arashdeep S. Thind<sup>b</sup>, Guodong Ren<sup>b</sup>, Rohan Mishra<sup>a, b</sup>, Katharine
- 4 M Flores a, b

1

2

9

22

23

24

25

26

27

28

29

30 31

32

33 34

35

- <sup>a</sup> Department of Mechanical Engineering and Materials Science, Washington University in St.
- 6 Louis, St. Louis, MO, 63130, USA
- 7 b Institute of Materials Science and Engineering, Washington University in St. Louis, St.
- 8 Louis, MO, 63130, USA

#### Abstract

- 10 The microstructure and mechanical properties of the equiatomic NbVZr alloy are reported.
- 11 The laser-processed and as-cast samples both exhibit a dendritic BCC solid solution with
- hexagonal C14 and cubic C15 Laves phases in the interdendritic regions. The stability of the
- 13 Laves phases is discussed based on first-principles total energy calculations. Nb is found to
- increase the stability of C14 and C15 phases. The Laves phases strengthen the material by
- 15 acting as obstacles to dislocation motion, as evidenced by nanoindentation and TEM
- observations of deformed samples. A high concentration of stacking faults was observed in
- 17 the Laves region, which confirms the low stacking fault energy predicted by first-principles
- 18 calculations, and are expected to result in additional plasticity. This work serves as an
- example of a systematic study of the stability of intermetallic phases in refractory complex
- 20 concentrated alloys using a high-throughput synthesis technique. Such phases play an
- 21 important role in the overall mechanical properties of the alloy.

## 1. Introduction

Complex concentrated alloys (CCAs) are solid solution alloys with equal or nearly equal concentrations of alloying elements and a lack of a dominant solvent species [1]. They provide a vast compositional space to discover novel properties and even design materials with contraindicative properties [2-4]. A special class of CCAs are refractory complex concentrated alloys (RCCAs) [5-8] that are attractive materials for high-temperature structural applications as they display an atypical combination of properties, including high melting point, high strength, ductility, toughness, and low density. RCCAs frequently include three or more refractory metals (Group IV-VI transition metals) in high (often equal) concentration with occasional additions of non-refractory metals such as Al [8]. A large fraction of the reported RCCAs display a single-phase BCC solid solution [8-10], which is a result of the BCC crystal structure of the refractory metals and their increasing solubility with maximized configurational entropy at equiatomic concentrations. More recently, RCCAs with secondary intermetallic phases, such as Laves and B2 structures, are garnering interest [11-16].

Similar to conventional BCC metals and alloys, the primary BCC solid solution in RCCAs results in high strength, but a lack of ductility at room temperature [1]. To improve the ductility of RCCAs, there have been attempts to alloy at least five principal elements, which increases the configurational entropy of mixing and prevents the formation of multiphase RCCAs with brittle intermetallic precipitates. However, in recent work on NbTiZr-based RCCAs, Senkov et al. [17] demonstrated that achieving a single solid solution phase does not necessarily lead to better mechanical properties. Compared to the single-phase BCC solid solution in NbTiZr, multi-phase NbTiZrVTa and NbTiZrVMo alloys exhibit superior yield strength at both room and elevated temperatures. Some multi-phase RCCAs, such as AlMo<sub>0.5</sub>NbTa<sub>0.5</sub>TiZr and their derivatives [18, 19], offer exceptional yield strength up to 1000 °C due to the presence of thermally stable nanoscale precipitates. Inspired by the microstructure of nickel superalloys ( $\gamma$ -FCC and  $\gamma$ '-L1<sub>2</sub> precipitates), Miracle and coworkers have proposed designing secondary particle-strengthened RCCAs with a good combination of strength and ductility [15, 20, 21]. However, there is a lack of studies focused on the stability of the intermetallic phases and how they affect the overall mechanical properties.

The above-mentioned work highlights the need to identify the competing intermetallic phases that may precipitate in RCCAs, the factors that stabilize the intermetallics, and their mechanical properties. In this work, we fabricate equimolar NbVZr RCCAs — which forms a base for several RCCAs — and use it as a prototype system to investigate the above questions. Although Zr and V are not included in the classical definition of refractory elements, they are included in the broader definition [22] and are common alloying elements in high-temperature materials. The ternary NbVZr alloy exhibits a dendritic microstructure consisting of a BCC solid solution, with two Laves structures forming in the interdendritic regions. In contrast to semi-empirical rules that largely predict the formation of a single BCC solid solution, we found the Laves phases to be thermodynamically and structurally stable based on total energy and phonon calculations using density-functional theory (DFT) in previous work [23]. We find that the secondary Laves phases strengthen the BCC phase by acting as obstacles to dislocation motion. Moreover, we observe a large concentration of stacking faults in the Laves phases due to their low stacking fault energy (SFE), which introduce additional plasticity during deformation. Finally, we apply laser processing to remelt and rapidly quench the material and obtain remarkable consistency with as-cast and annealed microstructures as well as their mechanical properties. This work demonstrates the viability of laser processing as a high-throughput screening technique for more complex RCCAs, and provides guidance for the application of laser additive manufacturing methods to this system.

### 2. Materials and Methods

#### 2.1 Sample preparation and experimental characterization

The raw materials (Nb, V and Zr) with purities of at least 99.8 wt. % were arc-melted on a water-cooled copper hearth in an argon atmosphere to produce six equiatomic alloy buttons each weighing approximately 15 g. Each button was flipped and remelted at least five times to improve compositional homogeneity. Subsequently, all six buttons were melted together and cast into a copper mold to produce  $20 \times 20 \times 5$  mm plates. To study the microstructure and properties in a more equilibrated state, an as-cast sample was annealed in a tube furnace

(Thermo Scientific Lindberg/Blue M) at 1100 °C for 72 h with a continuous argon flow to minimize oxidation. Finally, to examine a rapidly quenched state, an area of  $16 \times 16$  mm on the surface of an as-cast plate was melted using an Optomec MR-7 Laser Engineered Net Shaping (LENS<sup>TM</sup>) instrument. The laser power was 250 W, the travel speed was 6.35 mm/s and the spacing between adjacent laser tracks was 0.5 mm. There was approximately 25% overlap between adjacent laser tracks.

Cross sections of the as-cast and annealed samples and the surface of the laser-processed sample were cleaned, ground with up to 1200 grit sandpaper, and polished with  $0.02~\mu m~SiO_2$  solution. A total thickness of  $\sim 0.2~mm$  of the laser-processed material was removed by this metallographic preparation. In comparison, the depth of the laser-melted zone was on the order of 0.5~mm.

To identify the phases in the laser-processed, as-cast, and annealed materials, the polished surfaces were characterized with X-ray diffraction (XRD, Bruker d8 X-ray Diffractometer). Diffraction angles between 10° and 100° (20) were collected with a step size of approximately 0.02°. The plan-view microstructure was further characterized using a field emission scanning electron microscope (SEM, JEOL JSM-7001FLV) operated at 15 kV accelerating voltage, and the distribution of the crystallographic phases was mapped using electron backscatter diffraction (EBSD, Oxford Symmetry). The composition of the surface was determined using energy dispersive X-ray spectroscopy (EDS, Oxford Aztec Live X-Max Energy).

Further structural characterization of the laser-processed sample was conducted using (scanning) transmission electron microscopy ((S)TEM). TEM foils were sectioned and thinned with a ThermoFisher Scios 2 focused ion beam (FIB). For consistency, all of the cross-sectional foils were taken from the center of the laser tracks, and oriented perpendicular to the laser travel direction. A lower accelerating voltage of 5 kV was used in the final thinning step to reduce Ga<sup>+</sup> ion penetration into the sample. TEM observations were carried out using a JEOL JEM-2100F Field Emission (S)TEM. Atomic resolution STEM imaging and spectroscopy experiments were performed using the Nion UltraSTEM200 microscope at Oak Ridge National Laboratory. High-angle annular dark field (HAADF) Z-contrast imaging was performed using a probe convergence angle of 30 mrad and an annular dark-field detector with an inner angle larger than 80 mrad. Electron energy loss (EEL) spectrum imaging maps were collected using a Gatan Enfinium spectrometer with a collection semi-angle of 33 mrad and an energy dispersion of 0.25 eV, to obtain spatially resolved chemical maps of L<sub>2,3</sub> edges of V, Zr and Nb. A dwell time of 0.8 seconds/pixel was used for acquiring the V L<sub>2.3</sub> edge map while a dwell time of 4 seconds/pixel was used for acquiring the Zr and Nb L<sub>2,3</sub> edge maps. We performed principal component analysis (PCA) to improve the signal to noise ratio for the EELS datasets.

The mechanical properties of the constituent phases were examined with nanoindentation and dynamic modulus mapping using a Hysitron TI 950 Triboindenter equipped with a diamond Berkovich indenter tip. Nanoindentation was performed on the polished surface of laser-processed (plan view surface) and the cross sections of the as-cast and annealed samples at a loading and unloading rate of  $1000 \, \mu \text{N/s}$  up to a maximum load of  $5000 \, \mu \text{N}$ . The indents were spaced at least  $20 \, \mu \text{m}$  apart. Load-displacement data was used to determine the reduced modulus,  $E_r$ , and hardness, H, using the method developed by Oliver and Pharr [24]. The Young's modulus,  $E_r$ , was obtained from reduced modulus, using the equation:

$$\frac{1}{E_r} = \frac{1 - v^2}{E} + \frac{1 - v'^2}{E'}$$
 Eq. 1

where E' and v' are the Young's modulus and Poisson's ratio, respectively, of the diamond indenter tip, and v is the Poisson's ratio of the sample, which is assumed to be 0.4 in the calculation. Modulus maps with dimensions of 5  $\mu$ m × 5  $\mu$ m were collected using the nanoDMA function on the nanoindenter, with load amplitudes of 7 – 9  $\mu$ N and a load frequency of 200 Hz to achieve displacement amplitudes of 1 – 2 nm, which is sufficiently small to avoid plastic deformation [25].

## 2.2 Computational details

To investigate the stability of the experimentally observed Laves phases, we performed first-principles DFT calculations using the Vienna Ab initio Simulation Package (VASP) [26]. We employed generalized gradient approximation (GGA) as implemented in the Perdew-Burke-Ernzerhof (PBE) [27] exchange-correlation functional to approximate the many-body electronic interactions. We used the projector augmented-wave (PAW) method [28] to describe the core electrons with the following potentials: Nb\_pv for Nb, Zr\_sv for Zr, and V\_pv for V. For formation enthalpy ( $\Delta H_f$ ) calculations, we fixed the plane-wave energy cutoff at 400 eV and relaxed the structures until the forces on each atom were less than 0.01 eV Å<sup>-1</sup>. To model the disordered BCC solid solution, we generated special quasi-random structures (SQSs) [29] using the Alloy Theoretic Automated Toolkit (ATAT) [30]. For the 36-atom SQSs, we chose a  $4 \times 4 \times 1$   $\Gamma$ -centered k-points mesh for relaxation. For ordered C15 and C14 Laves structures, Monkhorst–Pack k-points mesh of size  $4 \times 4 \times 4$  and  $6 \times 6 \times 4$  were used, respectively. The formation enthalpy was calculated with respect to constituent elements:

$$\Delta H_f = E(A_x B_y C_z) - \frac{x}{x + y + z} E_{el}(A) - \frac{y}{x + y + z} E_{el}(B) - \frac{z}{x + y + z} E_{el}(C), \quad \text{Eq. 2}$$

where  $E(A_xB_yC_z)$  is the energy of the relaxed  $A_xB_yC_z$  compounds, and  $E_{el}$ 's are the energy of the constituent elements in their most stable crystal structure, which were calculated using the same convergence criteria as above.

To accurately calculate the elastic properties, we increased the cutoff energy to 700 eV and relaxed the structures to approximately zero stress (forces on ions <  $10^{-4}$  eV Å<sup>-1</sup>). Then, we applied small perturbations  $\delta \in \{-0.01, -0.005, +0.005, +0.01\}$  to the fully relaxed lattice vectors and calculated the resulting stress tensor. The 6 × 6 matrix of elastic constants was then calculated assuming a linear elastic constitutive relationship. From this, the bulk modulus (B) and shear modulus (G) were calculated using the Hill averaging scheme [31]. Young's modulus (E) and Poisson's ratio ( $\nu$ ) were obtained according to the following equations:

$$E = \frac{9BG}{3B + G}$$

$$v = \frac{3B - 2G}{2(3B + G)}$$
Eq. 3

For more details on the calculation of the elastic properties, please refer to Ref. 24.

To assess the energy of the stacking faults observed in the Laves phases, we built two atomistic models by intentionally adding 1-layer and 3-layer C15 structures into bulk C14

structures. Experimentally, we observe the composition of the Laves phases vary with local distortions and the exact elemental occupancies in Laves phases are unclear. Hence, we start by developing faulted structures with NbV<sub>2</sub> composition and tracked their energy change with incremental additions of Zr. We fully relaxed the faulted structures and define the stacking fault energy (SFE) as the energy difference of the faulted structure from the most stable C14 phase with identical composition.

#### 3. Results

#### 3.1 Microstructural characterization

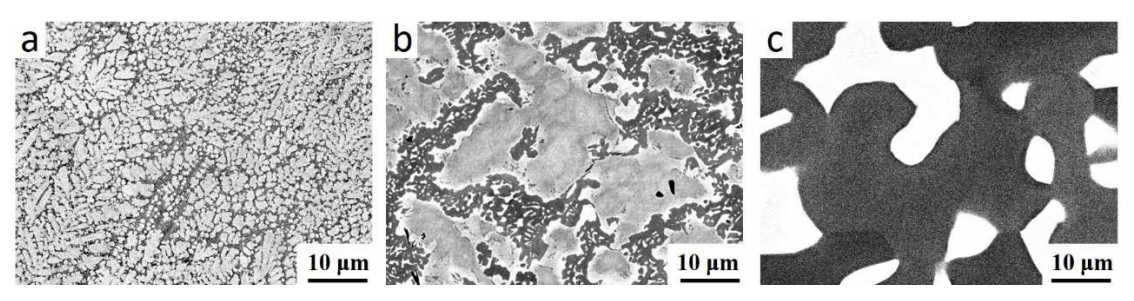


**Figure 1**. Backscattered electron images of (a) laser-processed, (b) as-cast, and (c) annealed NbVZr alloy.

Backscattered electron images of the laser-processed, as-cast, and annealed NbVZr alloys exhibit a dendritic microstructure, as shown in Figure 1. The dendrites are brighter in contrast, suggesting that they are enriched in heavier elements (Nb, Zr) compared with the darker interdendritic regions. We observed significant refinement of the microstructure in the laser-processed sample due to the inherently rapid cooling rate, which is approximately 2-5 orders of magnitude faster than cooling during the casting process, depending on the laser heat input [32]. As a result, the feature sizes in laser-processed sample are reduced by approximately 5 times relative to the as-cast, consistent with previous studies [33, 34]. Annealing results in a decrease in dendritic fraction and a commensurate coarsening of the interdendritic regions.

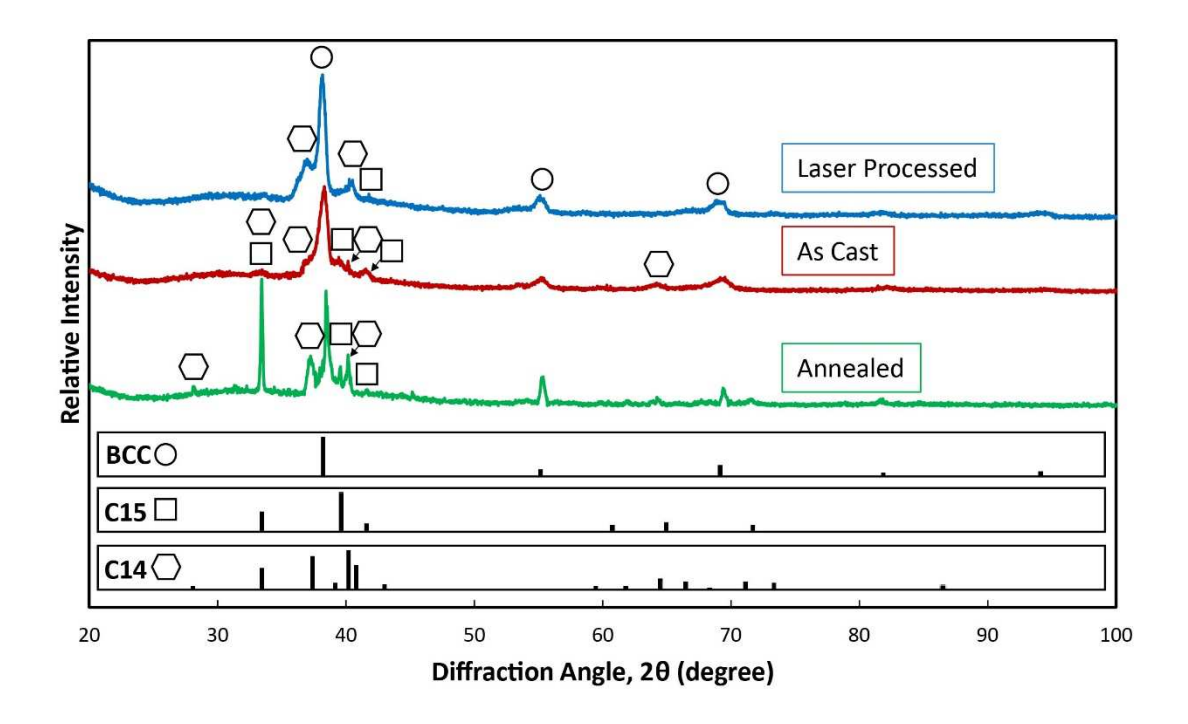


**Figure 2**. X-ray diffraction patterns of laser-processed, as-cast, and annealed equiatomic NbVZr samples indicate the existence of BCC, C14 (hexagonal Laves) and C15 (cubic Laves) phases. Reference BCC, C15 and C14 peaks are from a simulation of the corresponding structures with lattice parameters obtained from XRD.

We employed X-ray diffraction (XRD) to identify the phases present in laser-processed, as-cast, and annealed samples, as shown in Figure 2. Using this data, we confirmed the presence of BCC, C15 (cubic Laves) and C14 (hexagonal Laves) structures in all the three processing conditions. Their corresponding peaks are labeled with circles, squares, and hexagons, respectively. In all three samples, some expected peaks of the Laves phases are not observed in the spectra, most likely because we characterized the surface of a bulk sample rather than a powder specimen, which would present a more uniform distribution of crystallographic orientations. Note that the two small, broad peaks at 20 of approximately 53° and 60° correspond to the sample holder.

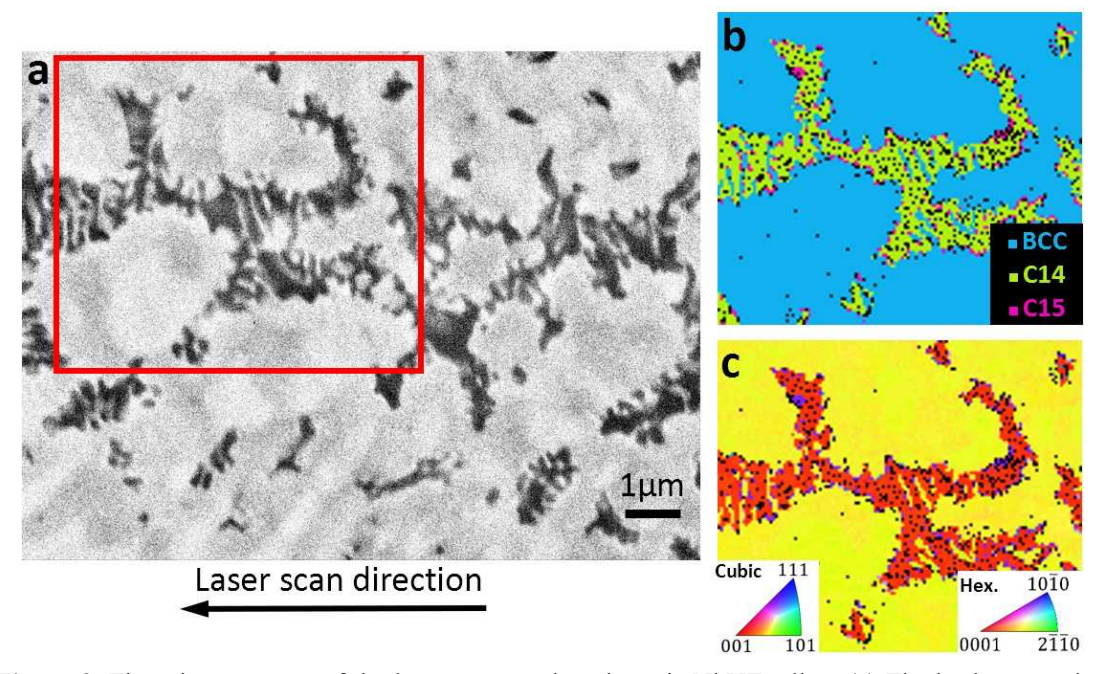


**Figure 3**. The microstructure of the laser-processed equiatomic NbVZr alloy. (a) The backscattered electron image. (b) The phase map constructed using EBSD indicates that the dendritic phase is BCC, while the C14 (hexagonal Laves) phases are primarily in the interdendritic regions. The C15 phase (cubic Laves) is confined at the phase boundaries between BCC and C14. (c) Inverse pole figure map showing uniform orientation within the phases. The black dots in (b) and (c) are unindexed EBSD measurements.

3

4 5

6

7 8

9

1011

12

13

14

15

16 17

18

19

20

21

We further employed EBSD to characterize the distribution of the phases, as shown in Figure 3 for the laser-processed specimen. A dendritic structure with secondary phase separation within the interdendritic regions is observed in backscattered electron images, as shown in Figure 3a. An EBSD phase map reveals the distribution of the BCC, C14, and C15 phases, as shown in Figure 3b, which corresponds to the highlighted area in Figure 3a. This data indicates that the dendritic phase is BCC while the interdendritic regions primarily consist of the C14 Laves phase. Minor amounts of isolated C15 are observed primarily at the BCC/C14 phase boundaries. Within the small area of observation, all of the phases exhibit uniform orientation as shown in Figure 3c. The orientation of C14 is in the vicinity of (0001), while C15 is close to (111). In the laser-processed specimen, we estimate the area fractions of the phases to be 80% BCC, 16% C14, and 4% C15. For the as-cast, the fraction of the BCC phase decreases to 41%, while the C14 increase to 53%. The C15 fraction increases only slightly, to 6%. Annealing further reduces the amount of BCC phase to 28%, while increasing the C14 to 67%, and the C15 again remains relatively constant at 5%. The average compositions of BCC phase, evaluated by SEM-EDS, are Nb<sub>34±6</sub>V<sub>25±2</sub>Zr<sub>41±7</sub>, Nb<sub>46±3</sub>V<sub>29±5</sub>Zr<sub>25±4</sub>, and Nb<sub>46±2</sub>V<sub>12±4</sub>Zr<sub>42±8</sub> for the laser-processed, as-cast, and annealed samples, respectively, where the errors are standard deviations from at least six measurements. The mean squared errors (MSE) between the BCC composition and the equiatomic composition (i.e., the overall composition), defined by MSE =  $\frac{1}{n}\sum (c_i - \bar{c})^2$  where  $c_i$  and  $\bar{c}$  are the individual and the mean concentrations, respectively, increase from 0.0047 for laser-processed sample, to 0.0010

and 0.025 for as-cast and annealed samples, respectively. The larger deviation in compositions indicates a more thorough element partitioning due to the longer equilibration time.



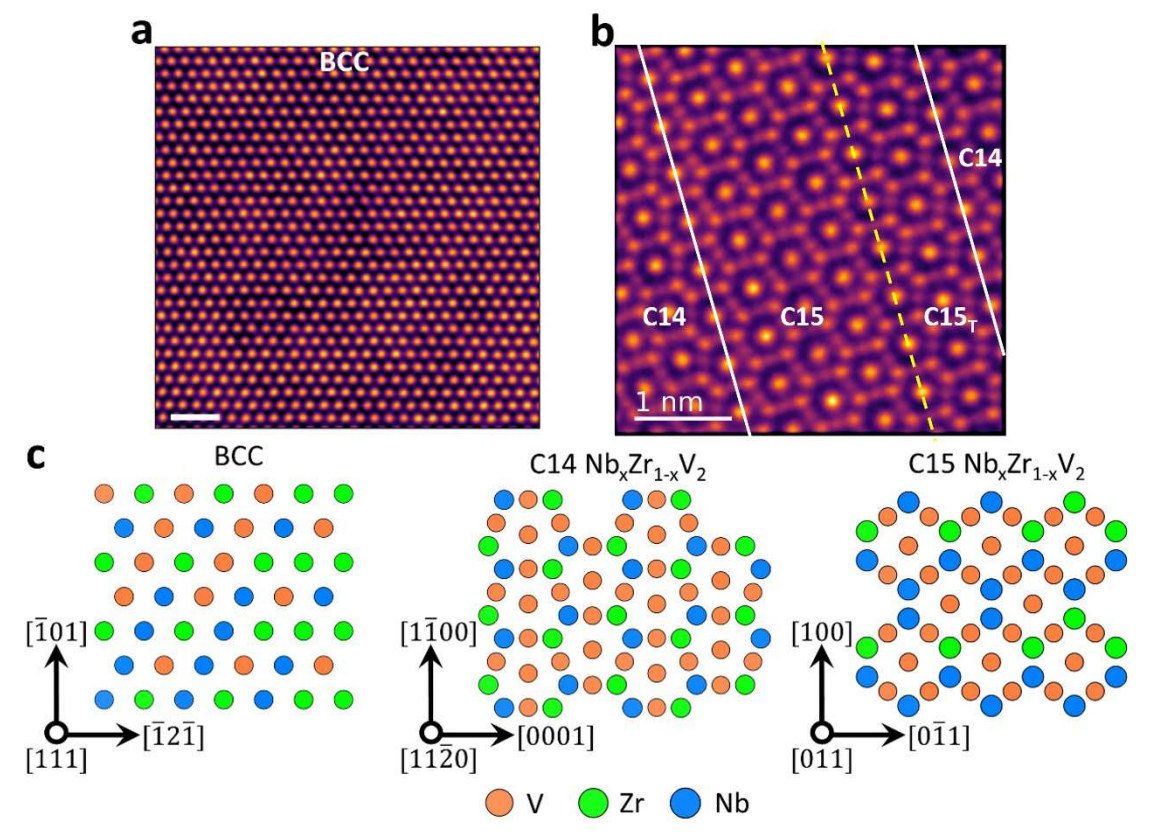


**Figure 4.** Atomic resolution HAADF images showing (a) BCC and (b) C14/C15 Laves phases. The white solid lines in (b) indicate stacking faults, and the yellow dashed line indicates a twin fault in C15. Readers are referred to Figure 10 for details of the defect structures. Scale bars in (a) and (b) correspond to 1 nm. (c) Representative atomic models of the BCC phase and the C14/C15 Laves phases with crystal structure orientations consistent with their corresponding HAADF images.

We performed atomic resolution STEM imaging to elucidate the atomic structure of the various phases in the laser-processed NbVZr alloy. Figure 4a shows an atomic resolution HAADF image of the BCC phase from the dendritic region, observed along the [111] direction. In a HAADF image, the intensity of an atomic column is approximately proportional to the square of the atomic number (~Z²) [35]. With the atomic density along the [111] orientation of BCC being equal for all the atomic sites, the uniform HAADF intensity for all the atomic columns indicates that the BCC dendrites are a disordered solid solution. Using HAADF-STEM imaging, we further confirm the formation of C14 and C15 Laves phases in the interdendritic regions, as shown in Figure 4b. We find alternating C14 and C15 phases are separated by stacking faults, highlighted as solid white lines in Figure 4b, and are hence coherent. The corresponding crystal structure orientations of the C14 and C15 Laves phases are provided in Figure 4c. These stacking faults are consistent with the orientation difference between the C14 and C15 phases observed in the EBSD image (Figure 3c).

We performed STEM-EELS to determine the spatial distribution of Nb, V and Zr across the dendritic and interdendritic regions. Figure 5a shows a wide field-of-view HAADF image

of the dendritic microstructure in the laser-processed NbVZr alloy sample, where the region chosen for EEL spectrum imaging is highlighted with a white box. The HAADF image simultaneously acquired during EELS acquisition, with dendritic (bright) and interdendritic (dark) regions, is shown in Figure 5b. From the elemental maps of V, Zr and Nb (shown in Figure 5c), we observe that the dendritic regions are rich in Nb and Zr whereas the interdendritic regions are rich in V. Extracted L<sub>2,3</sub> edges for V, Zr and Nb for the regions highlighted by blue, green and red squares in Figure 5b, are shown in Figure 5d. From SEM-based EDS measurements, we find that the average composition of the BCC phase is Nb<sub>34±6</sub>V<sub>25±2</sub>Zr<sub>41±7</sub>, while the overall composition is close to equiatomic, Nb<sub>32±1</sub>V<sub>34±1</sub>Zr<sub>34±2</sub>, which supports the conclusion from the EELS results that the dendritic regions are rich in Nb and Zr.

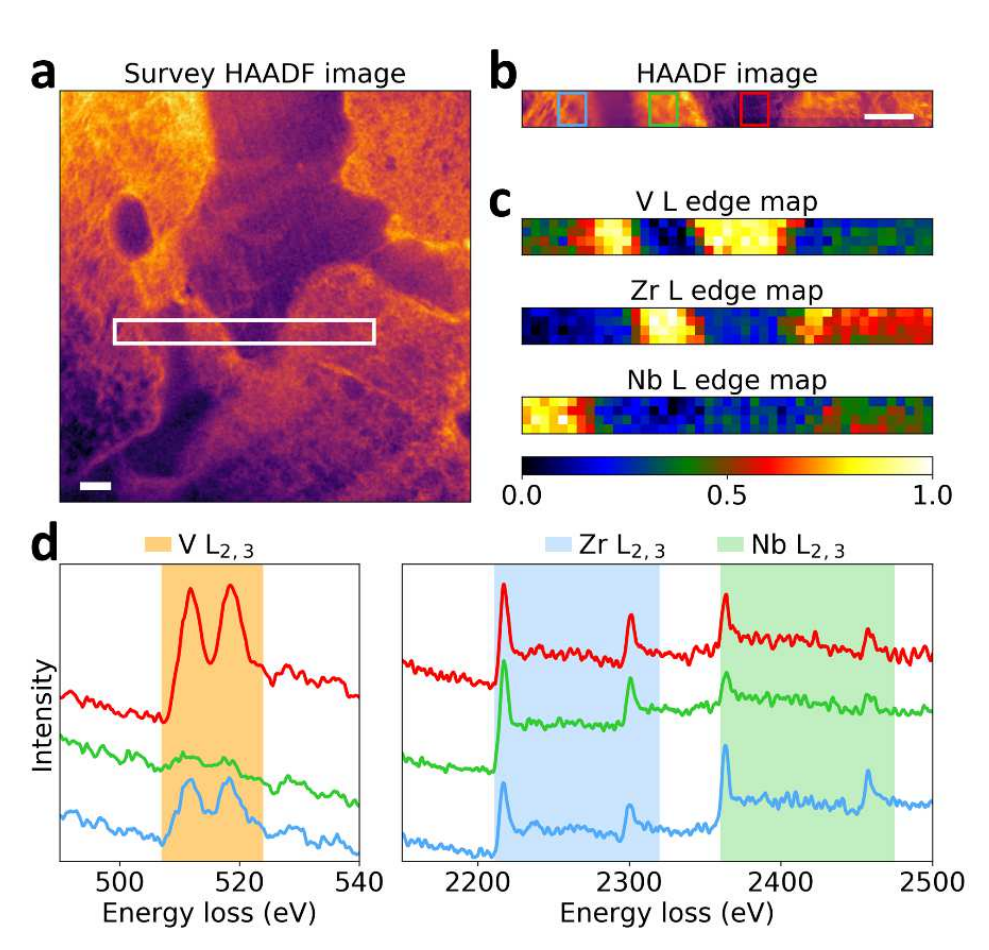


**Figure 5**. (a) A HAADF survey image with area chosen for EELS data acquisition highlighted with a white box. (b) Simultaneously acquired HAADF image of the region highlighted in (a). A  $16 \times 16$  sub-pixel scanning was enabled during EELS acquisition. Scale bars in (a) and (b) correspond to 100 nm. (c) Normalized V, Zr and Nb  $L_{2,3}$  edge maps. (d) EEL spectra for V, Zr and Nb extracted from the regions highlighted with corresponding colors in (b).

### 3.2 Mechanical properties

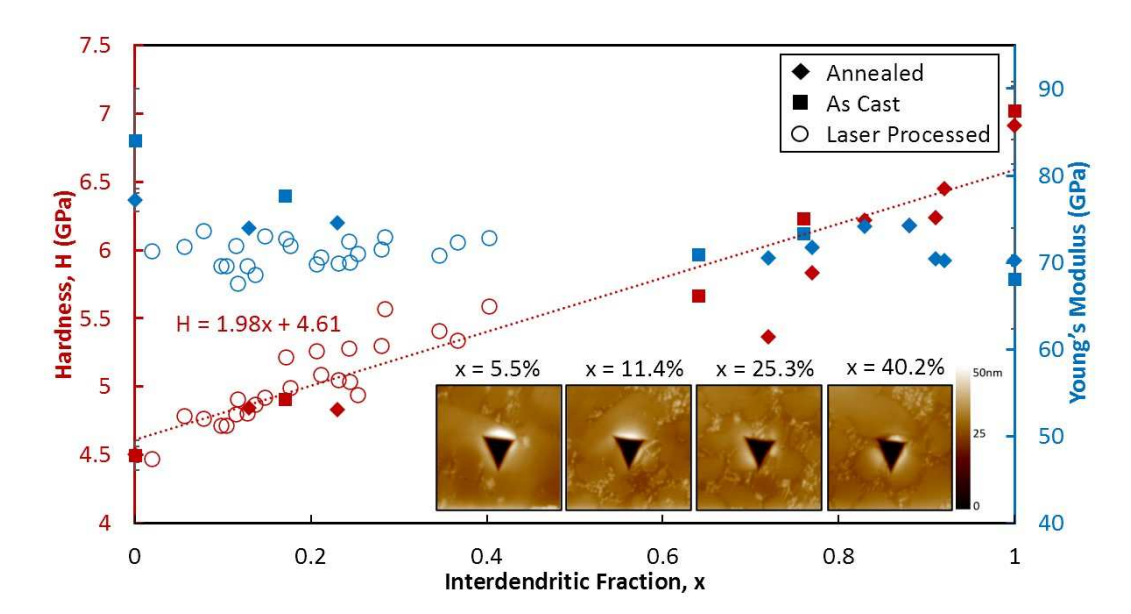


**Figure 6**. Hardness (red) and Young's modulus (blue) measured by nanoindentation as a function of interdendritic fraction. Insets are examples of scanning probe microscopy images showing the microstructures surrounding the indents with a scanning size of 5 μm.

We have characterized the mechanical properties of annealed, as-cast, and laser-processed samples via nanoindentation. Scanning probe microscopy (SPM) images of the surface topography, obtained using the nanoindenter probe prior to indentation, confirm the presence of a dendritic microstructure, and have been used to correlate the measured hardness and modulus values with the local microstructure. Noting that the diameter of the indentation sampling volume has been reported to be approximately four times the size of the indent [36], we assume that all of the phases within this sampling volume contribute to the mechanical properties, and further assume that the phase fractions within the volume can be represented by those present in a 4 µm diameter circular area centered on each 1 µm wide indent. The length scale in the refined laser-processed microstructures is on the microscale (Figure 1), so the sampling area generally includes both dendrites and interdendritic regions, while it is possible to sample fully dendritic or interdendritic regions in the as-cast and annealed materials. We estimated the relative fractions of the dendritic and interdendritic regions in a 4 µm diameter circular area around each indent position based on the contrast in the SPM

The hardness of the annealed, as-cast, and laser-processed material was found to increase linearly with interdendritic fraction, along the same trend line, as shown in Figure 6. In contrast, there is not a strong correlation between Young's modulus and interdendritic fraction in the laser-processed samples. The average Young's modulus is  $73.4 \pm 5.2$  GPa. However, the nanoindentation tests on the as-cast and annealed materials reveal a slight decreasing trend with interdendritic fraction. When the area of interest is fully dendritic (x = 0), the Young's moduli are  $84.0 \pm 6.0$  and  $77.2 \pm 1.3$  GPa for as-cast and annealed materials, respectively, and

images. The hardness and modulus values are plotted as a function of the area fraction of the

interdendritic material at the same position in Figure 6.

they decrease to  $68.1 \pm 5.8$  and  $70.3 \pm 0.6$  GPa when the indent is fully contained within the interdendritic region (x = 1). To better distinguish the properties of the BCC and Laves phases, dynamic modulus mapping was applied to map spatial variations in the storage modulus on the laser-processed sample. The variation in the storage modulus is compared with an SPM image of the same region in Figure 7. The dendritic regions clearly exhibit a higher storage modulus than the interdendritic regions.

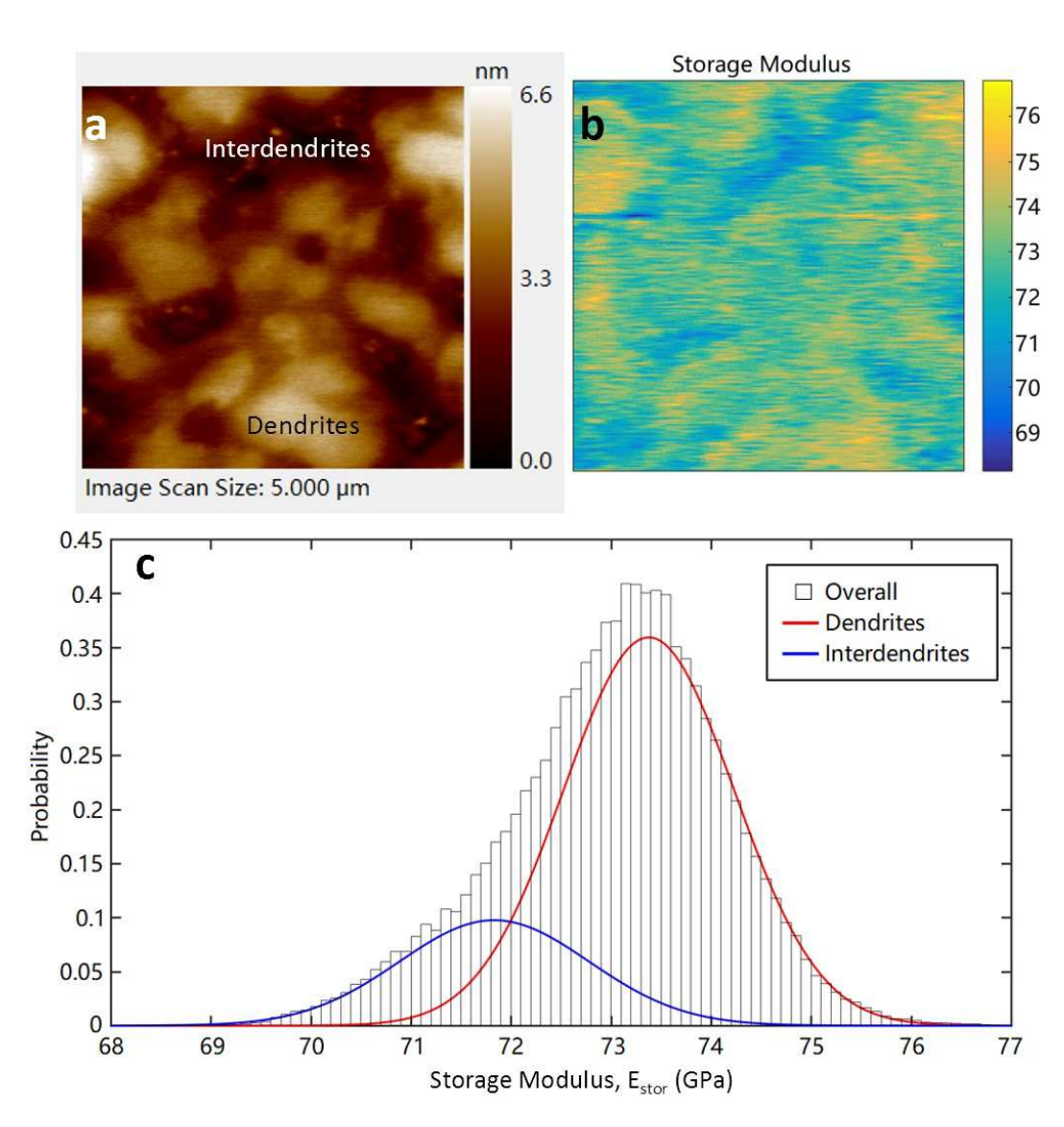


**Figure 7**. Dynamic modulus mapping. (a) A  $5 \times 5 \mu m^2$  SPM image, showing a dendritic microstructure; (b) the corresponding storage modulus map is measured at the same location; (c) overall storage modulus histogram, and the distributions for dendrites (red) and the interdendritic regions (blue), assuming the data can be fit by two Gaussian distributions.

1 2

3

4

5

6

7

## 4. Discussion

1

2

## 4.1 Phase stability

3 The competition between solid solution and intermetallic phases plays an important role 4 in determining the properties of CCAs. To date, several semi-empirical rules have been proposed for predicting the stability of disordered solid solution phases in CCAs [37-39], 5 including valence electron concentration (VEC =  $\sum c_i(VEC)_i$ ), mixing enthalpy ( $H^{SS}$  = 6  $\sum_{i < j} 4H_{ij}c_ic_j$ ), atomic size mismatch ( $\delta r = \sqrt{\sum c_i(1 - r_i/\bar{r})^2}$ ), and electronegativity 7 mismatch ( $\delta \chi = \sqrt{\sum c_i (\chi_i - \bar{\chi})^2}$ ), where  $c_i$ , (VEC)<sub>i</sub>,  $r_i$ , and  $\chi_i$  correspond to the 8 concentration, valence electron concentration, radius, and electronegativity of ith component, 9 respectively,  $\bar{r}$  and  $\bar{\chi}$  are the average radii and electronegativities across all components, 10 respectively, and  $H_{ij}$  is the mixing enthalpy of the binary solution of elements i and j. We 11 applied these four parameters to the Nb-V-Zr system and plot them as a function of 12 13 composition in Figure 8. While experimentally we observe NbVZr to form a multi-phase 14 alloy with a BCC solid solution as the majority phase, the different empirical rules give diverging estimates. At equimolar concentration, VEC is 4.67, HSS is -4 meV/atom (based 15 on Chen et al.'s models [40]), and  $\delta \chi$  is 0.135, all of which fall into a range where the 16 formation of a single-phase BCC solid solution is expected (VEC < 6.87 [41],  $-15 < H^{SS} < 5$ 17 kJ/mol [42] and  $0.10 < \delta \chi < 0.15$  [43]). However, the atomic size mismatch  $\delta r$  at the center 18 19 of the phase diagram is 8.1%, which is larger than the necessary condition for the formation 20 of a solid solution phase ( $\delta r \leq 6.6\%$  [44]), and thus this criterion predicts the presence of intermetallic compounds. 21

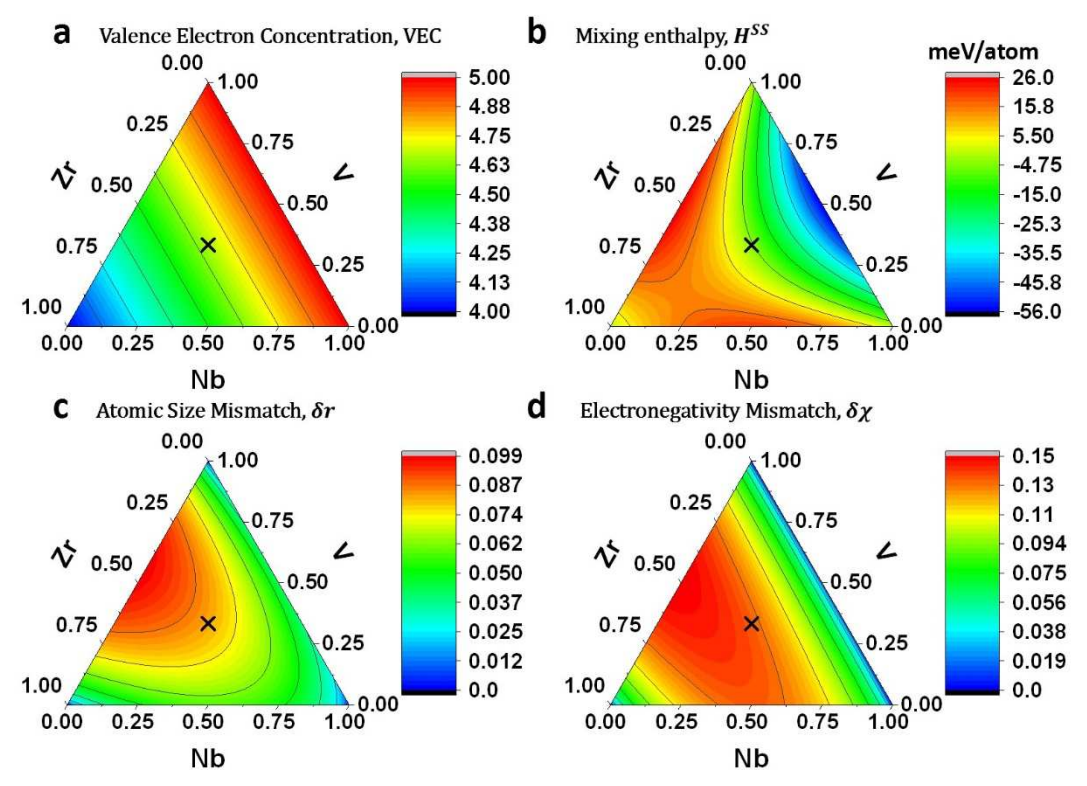


**Figure 8.** Ternary contour plots in Nb-V-Zr system of (a) valence electron concentration (VEC); (b) mixing enthalpy; (c) atomic size mismatch; (d) electronegativity mismatch. The equiatomic composition is marked with an X. The data used is from [1, 37, 40].

3

4

5 6

7

8

10

11

1213

14

15

16

17

18 19

20

2122

Based on the divergent predictions and their disagreement with experimental observations, the semi-empirical rules appear to be insufficient for determining the phase stability in the Nb-V-Zr system. We therefore conducted first-principles DFT calculations for a more accurate evaluation of the phase stabilities. For the BCC phase, we calculate its Gibbs free energy ( $\Delta G$ ) considering configurational entropy and mixing enthalpy, as shown in Figure 9a. While the equimolar NbVZr solid solution exhibits a  $\Delta H_f$  value of 0.127 eV/atom at 0 K, with increasing temperature,  $\Delta G$  reduces to -0.109 eV/atom at 2500 K, indicating that the ternary BCC phase can be stabilized with configurational entropy. On the other hand, no stable intermetallic compounds have been reported within this ternary phase diagram in either the Materials Project [45] or OQMD [46] databases, except for two metastable binary ZrV<sub>2</sub> Laves structures. In both structures, V atoms form a tetrahedron around Zr, with Zr atoms ordered either in a diamond cubic structure (C15-Laves) or in a hexagonal structure (C14-Laves). We found that substituting Nb atoms into the metastable ZrV<sub>2</sub> Laves structures stabilizes both phases by reducing  $\Delta H_f$ , as shown in Figure 9b. Starting from ZrV<sub>2</sub>, we interpolate Nb atom into the Zr sub-lattice and observe that  $\Delta H_f$  decreases from 0.024 eV/atom to -0.059 eV/atom for the C14 phase, and from 0.042 eV/atom to -0.045 eV/atom for the C15 phase. The stability of these two Laves phases is also predicted by a recent machine learning model [23].  $\Delta H_f$  appears to be negative at NbZr<sub>3</sub>V<sub>8</sub> for C14 and Nb<sub>5</sub>Zr<sub>3</sub>V<sub>16</sub> for C15. The C14 Laves phase has an overall lower  $\Delta H_f$  than C15, which is consistent with the EBSD measurements that show C14 is the major intermetallic phase and minor amounts of C15 are primarily observed at the BCC/C14 phase boundaries.

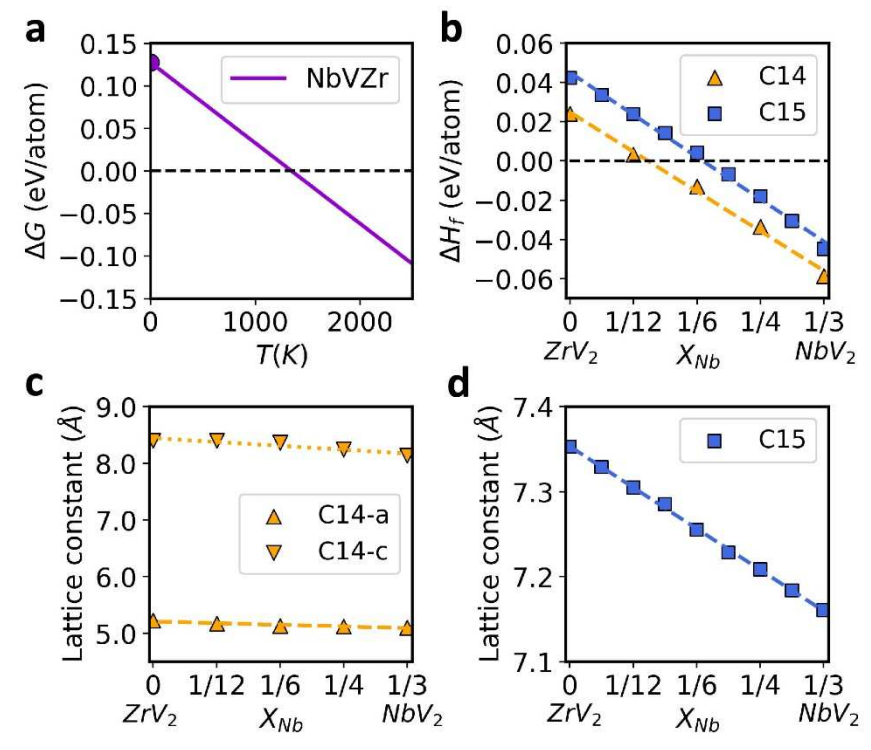


**Figure 9.** DFT-calculated formation enthalpies of (a) BCC solid solution of equimolar NbVZr, and (b) C14 and C15 structures of Nb<sub>x</sub>Zr<sub>1-x</sub>V<sub>2</sub> for x ranging from 0 to 1/3. The optimized lattice parameters of (c) C14 and (d) C15 Laves phases as a function of x.

The lattice parameters for both the Laves phases also decrease with Nb concentration following Vegard's rule [47], as shown in Figure 9c for the C14 phase and Figure 9d for the C15 phase. The calculated lattice constants of the C14 phase range from (a, c) = (8.40 Å, 5.22 Å) for ZrV<sub>2</sub> to (8.13 Å, 5.11 Å) for NbV<sub>2</sub>. Experimentally, XRD results indicate that the lattice constants are slightly larger, 8.48 Å and 5.33 Å. Similarly, DFT calculations underestimate lattice constant for the C15 phase. The calculated range is 7.35 – 7.16 Å, smaller than XRD measurements of 7.47 Å. This mismatch suggests the possible occupancy of larger Nb atoms on the V sub-lattice. We find that one Nb<sub>V</sub> substitutional defect in a 48-atom supercell of NbV<sub>2</sub> expands the volume by 0.103 Å<sup>3</sup>/atom. It increases  $\Delta H_f$  by 0.010 eV/atom, which is small enough to be stabilized by configurational entropy at the high processing temperatures.

Experimentally, we observe the C14 and C15 phases to be divided by parallel stacking faults in the interdendritic regions, as shown in Figure 4b, which indicates a high density of straight and parallel defects on  $(1\bar{1}1)_{C15}$  and  $(0001)_{C14}$  planes. Figure 10 shows a schematic of the defect structure, with each sub-layer of atoms in a unit block labeled. For a Laves structure  $XY_2$ , the capital Latin letters (A, B, C) identify a single layer with a Kagome lattice of Y atoms, which are accompanied by three neighboring sub-layers, identified by small Greek letters  $(\alpha, \beta, \gamma)$  denoting X atoms and small Latin letters (a, b, c) denoting Y atoms. Along [0001] for C14 or [1 $\bar{1}1$ ] for C15, these four adjacent layers form a basic unit block, denoted by script letters (e.g.  $\mathcal{A} = A\alpha c\beta$ ), with the stoichiometric ratio of  $XY_2$ . The cubic C15 Laves structure is similar to FCC with the  $\mathcal{ABC}$  stacking sequence of the unit blocks, while hexagonal C14 is similar to HCP with  $\mathcal{AB'AB'}$  type stacking. The primed

labels indicate a transformed unit block from the original by a synchroshear process, in which two sub-layers simultaneously shear in different directions. For instance,  $\mathcal{A}$  (A $\alpha c \beta$ ) becomes  $\mathcal{A}'$  (A $\alpha b \gamma$ ) when the  $\beta$  and c sub-layers each move by a Burger's vector,  $1/6[2\overline{1}1]$  and  $1/6[1\overline{2}1]$ , respectively. In the Laves phases, stacking faults or twin faults can form by means of synchroshear with a smaller energy cost than conventional dislocation slip [48].

1

2

3

4

5

6

7

8

9

10

11

12

13

1415

16

1718

19 20

2122

23

2425

26 27

28

29

30

31

In Figure 4b and Figure 10, the two solid lines (① and ③) denote stacking faults that divide the area of observation into regions where the unit blocks stack to form C14 or C15 phases. The dashed line (②) indicates a twin fault in the C15 phase. It is rare to see stacking faults and twin faults in such close proximity in a Laves intermetallic alloys. It is generally accepted that high lattice distortion energy favors the formation of stacking faults [49]. To further examine this, we built faulted structure models with 1 unit block and 3 unit blocks of C15 stacked parallel to C14 structures, as observed in the STEM images (e.g. Figure 4b). For NbV<sub>2</sub>, both of the models have low stacking fault energies (SFE) of 0.016 eV/atom for the 1 unit block stacking fault and 0.010 eV/atom for the 3 unit block stacking fault. Upon interpolating Zr into these faulted structures with an atomic ratio of ~20%, SFE remains relatively low at 0.067 eV/atom for 1 unit block faults and 0.038 eV/atom for 3 unit block faults. A low SFE is expected to affect the plastic response of the material by favoring the formation of partial dislocations and activating mechanical twinning when strained. The stacking faults observed in the present Nb-V-Zr alloy are similar to those reported in Hf<sub>13</sub>Nb<sub>25</sub>V<sub>62</sub> alloys by Luzzi et al. [50], wherein extensive C14/C15 stacking faults were observed. The SFE of C15 can be reduced by alloying [51]. In Luzzi et al.'s work [50], increasing the V content in the Hf-Nb-V system pushed the alloy towards the C14-stable region in the phase diagram, reducing the energy difference between a correct packing sequence (C15) and an incorrect sequence (C14) of (111) layers.

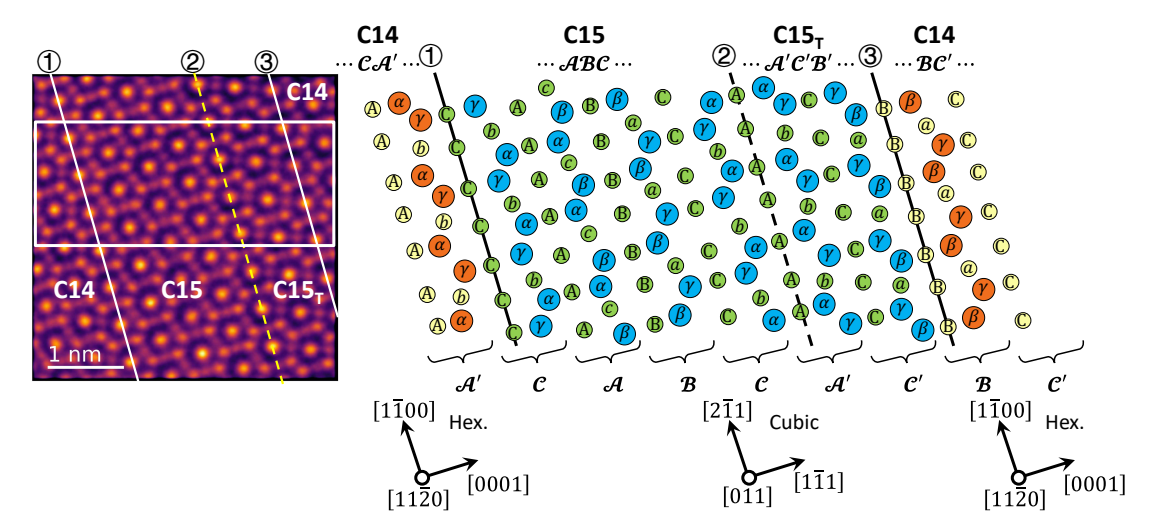


**Figure 10**. The atomic structure observed within the highlighted region of the HAADF image (left) is described schematically (right). Refer to the corresponding text for the meaning of the Latin, Greek, and script letters. The two solid lines (denoted by ① and ③) indicate two stacking faults that divide different crystal structures (orange/yellow for C14 and blue/green for C15). The dashed line (denoted by ②) indicates a twin fault in C15.

#### 4.2 Mechanical properties

In Figure 6, the Young's modulus of the BCC dendrites in the as-cast material, is markedly higher than that of the laser-processed or annealed materials. The modulus value of the laser-processed sample is slightly lower than the annealed. The higher as-cast modulus may be due to compositional differences in the BCC phase, which has much lower Zr content than the other two conditions. The rule of mixtures (ROM) of the moduli is defined by [52]

$$E_{ROM} = \frac{\sum_{i} c_i V_i E_i}{\sum_{i} c_i V_i}$$
 Eq. 5

where  $c_i$ ,  $V_i$ , and  $E_i$  are the *i*th constituent's concentration, molar volume, and Young's modulus, respectively. Based on the BCC compositions obtained from SEM-EDS measurements and elemental data from [1], Equation 5 estimates that the modulus of the as-cast material would be 98.2 GPa, while that of the laser-processed and annealed would be 90.7 GPa and 88.6 GPa, respectively. While ROM does not explain the smaller difference between the laser-processed and annealed material, the slightly higher modulus observed in the annealed state is consistent with the observed differences in lattice parameter, as calculated from the XRD data in Figure 2, where the BCC lattice parameter decreases from 3.35 Å to 3.31 Å with equilibration time.

The two Laves structures could not be distinguished from each other in SPM images (Figure 7a), although the BCC dendrites and the C14/C15 interdendritic regions could be distinguished based on their topography. Comparing Figure 7a and b, the regions with the higher storage modulus corresponds to the BCC dendrites, while the interdendritic regions have a lower storage modulus. The higher storage modulus of the BCC phase is consistent with the higher Young's modulus observed via nanoindentation (Figure 6). As can be seen in Figure 7c, the distribution of storage moduli obtained via dynamic modulus mapping could be split into 2 distinct Gaussian distributions using the Gaussian mixture model as implemented in MATLAB. In the software, a k-means clustering algorithm is used to select the initial parameters, and then the iterative Expectation-Maximization algorithm is employed to optimize the model [53]. The two distributions are centered at 71.8 GPa and 73.3 GPa, corresponding to the interdendritic regions and the dendrites, respectively. The area fractions of the map under each peak of the histogram are 77% for the higher peak and 23% for the lower peak. This area fraction agrees with the EBSD data in Figure 3, where the BCC phase makes up approximately 80% of the area.

As shown in Table 1, the theoretically predicted value of Young's modulus for the BCC phase with equiatomic composition falls between the average nanoindentation value and the average storage modulus measured in the dendrites. The elastic constants of the Laves phases were also calculated for the compositions noted in Table 1. These compositions were estimated based on EDS and EELS measurements, which indicated that interdendritic region are rich in V compared to the BCC phase. C14 and C15 are both more compliant compared to the BCC solid solution, consistent with the experimental results. The measured moduli are more consistent with the calculated Young's modulus for C14, since C14 was the majority phase in the interdendritic region. Our DFT calculations indicate that the elastic modulus of Laves phases is dependent on the atomic ratio and occupancy of Zr atoms. For instance, The theoretical Young's modulus of C14-Laves with composition NbV<sub>2</sub>, NbZrV<sub>2</sub> (Zr on Nb

7

8

9

10

11

12

13

1415

16

17

18

19 20

21

22

23

24

25

2627

28

1

sub-lattice) and NbVZr (Zr on V sub-lattice) are 108.9 GPa, 76.9 GPa, and 87.3 GPa, respectively. Local distortion induced by alternating C14/C15 stacking faults can also affect the overall elastic modulus.

**Table 1.** Young's (E), bulk (B), and shear (G) moduli and Poisson's ratio ( $\nu$ ), calculated with DFT for the compositions given in parentheses, are compared with experimentally obtained average modulus values for the dendritic (BCC) and interdendritic (C14/C15) regions.

	Experimental			DFT Calculations			
	E <sub>annealed</sub> *	E <sub>as-cast</sub> *	E <sub>stor, laser-processed</sub> *	Е	В	G	
	(GPa)	(GPa)	(GPa)	(GPa)	(GPa)	(GPa)	ν
C14				76.9	159.1	27.1	0.42
(NbZrV <sub>2</sub> )	70.3	68.1	71.8	70.9	139.1	27.1	0.42
C15	70.3	06.1	71.8	32.3	125.9	11.09	0.46
(NbZrV <sub>2</sub> )							
BCC	77.2	84.0	73.3	82.1	120.8	29.6	0.39
(NbVZr)	, , .2	00	, 3.3	02.1	120.0	27.0	0.57

<sup>\*</sup>E<sub>annealed</sub> and E<sub>as-cast</sub> were measured with nanoindentation. E<sub>stor, laser-processed</sub> was obtained from the mean of the corresponding Gaussian distributions fitted by the Gaussian mixture model.

As noted in Figure 6, the hardness of the annealed, as-cast, and laser-processed material increase linearly with the amount of interdendritic material included in the nanoindentation sampling volume. To investigate the corresponding deformation mechanism, we examined the microstructure of the laser-processed sample with multi-beam bright field TEM, shown in Figure 11. Figure 11a shows an undeformed region, where two Laves particles with different crystallographic orientations are observed embedded in the BCC matrix. The inset shows the electron diffraction pattern from the [110]<sub>C15</sub> zone axis of the particle labeled Laves I. Note that the diffraction spots are sharp and distinct. Figure 11b shows the deformed microstructure in the vicinity of a nanoindent. A high concentration of entangled dislocations is observed inside the BCC matrix, and dislocation pileups are observed at the interphase boundary. In the Laves phase, the prominent streaking of the diffraction spots along {111}<sub>C15</sub>//(0001)<sub>C14</sub> provides evidence of the high density of stacking faults after deformation. In contrast to single screw dislocation glide in the BCC structure [9, 54, 55], dislocation nucleation in Laves phases is difficult as it is closely related to the formation of unstable stacking faults, where the sub-layers are displaced by a half Burger's vector as opposed to a full Burger's vector to form a stable stacking fault [56-58]. A first-principles study [48] indicated that the energy required to form these unstable stacking faults via synchroshear is large, albeit reduced relative to conventional slip. Additionally, due to complicated structures of the Laves phases, the propagation of dislocations is also difficult. Thus, the interphase boundary acts as an obstacle to dislocation motion, and the dislocation pileup necessary to generate the (stable) stacking faults in the Laves phase contributes to the enhanced strength (hardness) as the interdendritic fraction increases (Figure 6).

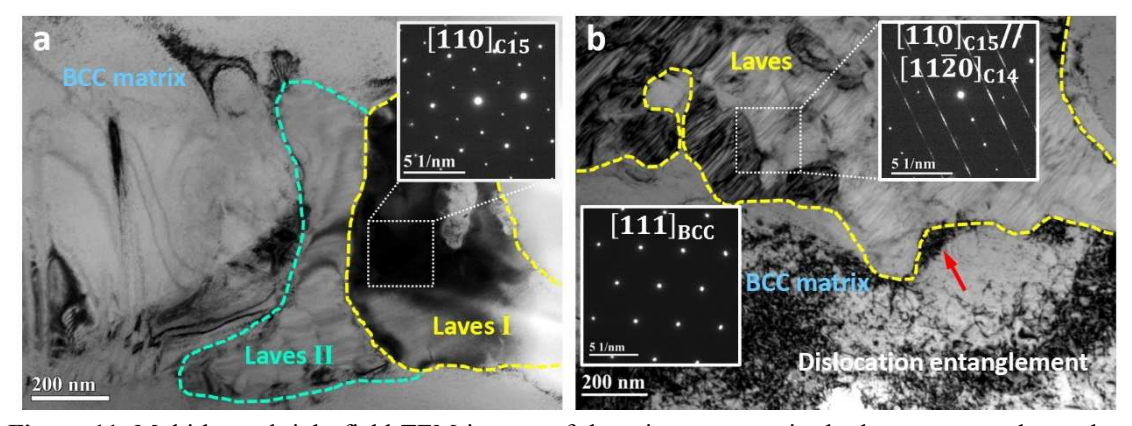


**Figure 11**. Multi-beam bright field TEM images of the microstructure in the laser-processed sample. (a) Prior to deformation: Two Laves particles (Laves I and Laves II) with different orientations are embedded in the BCC matrix. The electron diffraction pattern is taken from the  $[110]_{C15}$  zone axis. (b) Deformed microstructure near a nanoindent: The electron diffraction pattern taken from the  $[110]_{C15}$  //  $[11\bar{2}0]_{C14}$  zone axis indicates prominent streaking spots along zone axis  $\{111\}_{C15}$ //(0001) $_{C14}$ , which indicates a high density of stacking faults. A high concentration of entangled dislocations is observed inside the BCC matrix and an example of dislocation pile up at the interphase boundary is indicated by the red arrow.

Unlike the microstructure we observe in the present study, several compositions in the Hf-Nb-V and Cr-Nb-V refractory systems have been reported to form a dendritic C15 majority phase with BCC as the minor interdendritic phase [59-63]. Although Livingston and Hall [64] pointed out that twinning as well as dislocation motion accommodate deformation in C15 phases, these alloys with substantial fraction of Laves phases showed limited plasticity (< 5%) at low temperature. As described above, in the present work, the mechanical properties of NbVZr are mainly governed by the more ductile BCC phase, while the Laves phases strengthen the alloy.

As widely reported in elemental FCC metals, lowering the SFE in C15 phase increases the chance of deformation twinning, which can act as an additional deformation mode and increase the ductility of the alloy [65]. While low SFE structures are observed in some interdendritic regions in the present work, how these microstructures influence the mechanical properties at a larger scale requires further investigation. However, as shown in this study, by tailoring the composition to adjust the amount of C14 and C15 Laves phases, the Nb-V-Zr alloys have potential to act as a model system for investigating deformation mechanisms in multi-phase RCCAs.

#### 5. Conclusion

The structures and mechanical properties of an equiatomic NbVZr complex concentrated alloy were studied in the annealed, as-cast, and laser-processed conditions, as part of an effort to develop laser processing as a high-throughput synthesis method for screening potential RCCAs. The configurational entropy of the three-component system is not sufficient to stabilize a single-phase BCC solid solution. In addition to a dendritic BCC phase, two Laves

- 1 phases are observed in the interdendritic regions: a continuous hexagonal C14 phase and
- 2 isolated regions of cubic C15 phase. First-principles calculations indicate that Nb additions
- 3 increase the stability of the C14 and C15 phases. Nanoindentation measurements and TEM
- 4 observations indicate that the Laves phases strengthen the material, as dislocations pile up at
- 5 the interphase boundary between the softer BCC dendrites and the C14/C15 interdendritic
- 6 regions, resulting in the creation of stacking faults in the Laves phase. The SFE was found to
- 7 range from 0.038 eV/atom (for 3 unit block stacking fault) to 0.067 eV/atom (for 1 unit block
- 8 stacking fault), as obtained from first-principles calculations. The low SFE suggests
- 9 deformation twinning may be a possible deformation mode in the brittle Laves phases, which
- 10 requires further investigation. This alloy system can serve as a prototype to investigate the
- competition between random solid solutions and intermetallics, as well as the competition of
- different Laves phases, and their effect on the mechanical properties. Furthermore, the NbVZr
- alloy serves as a starting point for more comprehensive studies of RCCAs that have potential
- 14 for high-temperature applications by taking advantage of thermally stable nanoscale
- precipitation and the low SFE structures tailored by compositions and processing conditions.

## Acknowledgements

16

25

- 17 This work was supported by the National Science Foundation (NSF) under Grant No.
- 18 DMR-1809571. A.S.T. and G.R. were supported through NSF Grant No. DMR-1806147.
- 19 STEM experiments were conducted at the Center for Nanophase Materials Sciences at Oak
- 20 Ridge National Laboratory. DFT calculations in this work used computational resources of the
- 21 Extreme Science and Engineering Discovery Environment (XSEDE), which is supported by
- 22 NSF through Grant No. ACI-1548562. The authors acknowledge financial support from
- 23 Washington University in St. Louis and the Institute of Materials Science and Engineering for
- the use of shared instruments and staff assistance.

#### References

- 26 [1] D.B. Miracle, O.N. Senkov, A critical review of high entropy alloys and related concepts,
- 27 Acta Mater. 122 (2017) 448-511.
- 28 [2] Y.-S. Huang, L. Chen, H.-W. Lui, M.-H. Cai, J.-W. Yeh, Microstructure, hardness,
- 29 resistivity and thermal stability of sputtered oxide films of AlCoCrCu0.5NiFe high-entropy
- alloy, Materials Science and Engineering: A 457(1-2) (2007) 77-83.
- 31 [3] B. Cantor, I.T.H. Chang, P. Knight, A.J.B. Vincent, Microstructural development in
- 32 equiatomic multicomponent alloys, Materials Science and Engineering: A 375-377 (2004)
- 33 213-218.
- 34 [4] J.W. Yeh, S.K. Chen, S.J. Lin, J.Y. Gan, T.S. Chin, T.T. Shun, C.H. Tsau, S.Y. Chang,
- 35 Nanostructured High-Entropy Alloys with Multiple Principal Elements: Novel Alloy Design
- 36 Concepts and Outcomes, Advanced Engineering Materials 6(5) (2004) 299-303.
- 37 [5] O.N. Senkov, G.B. Wilks, D.B. Miracle, C.P. Chuang, P.K. Liaw, Refractory high-entropy
- 38 alloys, Intermetallics 18(9) (2010) 1758-1765.

- 1 [6] O.N. Senkov, G.B. Wilks, J.M. Scott, D.B. Miracle, Mechanical properties of
- 2 Nb25Mo25Ta25W25 and V20Nb20Mo20Ta20W20 refractory high entropy alloys,
- 3 Intermetallics 19(5) (2011) 698-706.
- 4 [7] S. Gorsse, J.-P. Couzinié, D.B. Miracle, From high-entropy alloys to complex
- 5 concentrated alloys, Comptes Rendus Physique 19(8) (2018) 721-736.
- 6 [8] O.N. Senkov, D.B. Miracle, K.J. Chaput, J.-P. Couzinie, Development and exploration of
- 7 refractory high entropy alloys—A review, Journal of Materials Research 33(19) (2018)
- 8 3092-3128.
- 9 [9] L. Lilensten, J.P. Couzinié, L. Perrière, A. Hocini, C. Keller, G. Dirras, I. Guillot, Study of
- 10 a bcc multi-principal element alloy: Tensile and simple shear properties and underlying
- deformation mechanisms, Acta Mater. 142 (2018) 131-141.
- 12 [10] J. Chen, X. Zhou, W. Wang, B. Liu, Y. Lv, W. Yang, D. Xu, Y. Liu, A review on
- 13 fundamental of high entropy alloys with promising high-temperature properties, Journal of
- 14 Alloys and Compounds 760 (2018) 15-30.
- 15 [11] J.P. Couzinie, O.N. Senkov, D.B. Miracle, G. Dirras, Comprehensive data compilation on
- the mechanical properties of refractory high-entropy alloys, Data Brief 21 (2018) 1622-1641.
- 17 [12] N.Y. Yurchenko, N.D. Stepanov, S.V. Zherebtsov, M.A. Tikhonovsky, G.A. Salishchev,
- Structure and mechanical properties of B2 ordered refractory AlNbTiVZr x (x = 0-1.5)
- 19 high-entropy alloys, Materials Science and Engineering: A 704 (2017) 82-90.
- 20 [13] B. Gorr, F. Mueller, H.-J. Christ, H. Chen, A. Kauffmann, R. Schweiger, D.V. Szabó, M.
- 21 Heilmaier, Development of Oxidation Resistant Refractory High Entropy Alloys for High
- 22 Temperature Applications: Recent Results and Development Strategy, TMS 2018 147th
- 23 Annual Meeting & Exhibition Supplemental Proceedings2018, pp. 647-659.
- 24 [14] O.N. Senkov, S.V. Senkova, D.B. Miracle, C. Woodward, Mechanical properties of
- 25 low-density, refractory multi-principal element alloys of the Cr–Nb–Ti–V–Zr system,
- 26 Materials Science and Engineering: A 565 (2013) 51-62.
- 27 [15] V. Soni, B. Gwalani, T. Alam, S. Dasari, Y. Zheng, O.N. Senkov, D. Miracle, R. Banerjee,
- 28 Phase inversion in a two-phase, BCC+B2, refractory high entropy alloy, Acta Mater. 185
- 29 (2020) 89-97.
- 30 [16] S. Laube, H. Chen, A. Kauffmann, S. Schellert, F. Müller, B. Gorr, J. Müller, B. Butz,
- 31 H.-J. Christ, M. Heilmaier, Controlling crystallographic ordering in Mo-Cr-Ti-Al high
- entropy alloys to enhance ductility, Journal of Alloys and Compounds 823 (2020).
- 33 [17] O.N. Senkov, S. Rao, K.J. Chaput, C. Woodward, Compositional effect on microstructure
- and properties of NbTiZr-based complex concentrated alloys, Acta Mater. 151 (2018)
- 35 201-215.
- 36 [18] O.N. Senkov, J.K. Jensen, A.L. Pilchak, D.B. Miracle, H.L. Fraser, Compositional
- 37 variation effects on the microstructure and properties of a refractory high-entropy superalloy
- 38 AlMo0.5NbTa0.5TiZr, Materials & Design 139 (2018) 498-511.
- 39 [19] J.K. Jensen, B.A. Welk, R.E.A. Williams, J.M. Sosa, D.E. Huber, O.N. Senkov, G.B.
- 40 Viswanathan, H.L. Fraser, Characterization of the microstructure of the compositionally
- complex alloy Al1Mo0.5Nb1Ta0.5Ti1Zr1, Scripta Materialia 121 (2016) 1-4.
- 42 [20] D.B. Miracle, Critical Assessment 14: High entropy alloys and their development as
- 43 structural materials, Materials Science and Technology 31(10) (2015) 1142-1147.

- 1 [21] D. Miracle, J. Miller, O. Senkov, C. Woodward, M. Uchic, J. Tiley, Exploration and
- 2 Development of High Entropy Alloys for Structural Applications, Entropy 16(1) (2014)
- 3 494-525.
- 4 [22] L.L. Snead, D.T. Hoelzer, M. Rieth, A.A.N. Nemith, Refractory Alloys: Vanadium,
- 5 Niobium, Molybdenum, Tungsten, Structural Alloys for Nuclear Energy Applications 2019, pp.
- 6 585-640.
- 7 [23] Z. Zhang, M. Li, K. Flores, R. Mishra, Machine learning formation enthalpies of
- 8 intermetallics, Journal of Applied Physics 128(10) (2020).
- 9 [24] W.C. Oliver, G.M. Pharr, Measurement of hardness and elastic modulus by instrumented
- indentation: Advances in understanding and refinements to methodology, Journal of Materials
- 11 Research 19(1) (2011) 3-20.
- 12 [25] P. Tsai, K. Kranjc, K.M. Flores, Hierarchical heterogeneity and an elastic microstructure
- observed in a metallic glass alloy, Acta Mater. 139 (2017) 11-20.
- 14 [26] G. Kresse, J. Furthmuller, Efficient iterative schemes for ab initio total-energy
- calculations using a plane-wave basis set, Phys Rev B Condens Matter 54(16) (1996)
- 16 11169-11186.
- 17 [27] J.P. Perdew, K. Burke, M. Ernzerhof, Generalized Gradient Approximation Made Simple,
- 18 Phys Rev Lett 77(18) (1996) 3865-3868.
- 19 [28] P.E. Blochl, Projector augmented-wave method, Phys Rev B Condens Matter 50(24)
- 20 (1994) 17953-17979.
- 21 [29] A. Zunger, S. Wei, L.G. Ferreira, J.E. Bernard, Special quasirandom structures, Phys. Rev.
- 22 Lett. 65(3) (1990) 353-356.
- 23 [30] A. van de Walle, M. Asta, G. Ceder, The Alloy Theoretic Automated Toolkit: A user
- 24 guide, Calphad 26(4) (2002) 539-553.
- 25 [31] R. Gaillac, P. Pullumbi, F.X. Coudert, ELATE: an open-source online application for
- analysis and visualization of elastic tensors, J Phys Condens Matter 28(27) (2016) 275201.
- 27 [32] I. Kunce, M. Polanski, K. Karczewski, T. Plocinski, K.J. Kurzydlowski, Microstructural
- 28 characterisation of high-entropy alloy AlCoCrFeNi fabricated by laser engineered net shaping,
- 29 Journal of Alloys and Compounds 648 (2015) 751-758.
- 30 [33] M. Li, K.M. Flores, Laser processing as a high-throughput method to investigate
- 31 microstructure-processing-property relationships in multiprincipal element alloys, Journal of
- 32 Alloys and Compounds 825 (2020) 154025-154025.
- 33 [34] M. Li, J. Gazquez, A. Borisevich, R. Mishra, K.M. Flores, Evaluation of microstructure
- and mechanical property variations in AlxCoCrFeNi high entropy alloys produced by a
- 35 high-throughput laser deposition method, Intermetallics 95 (2018) 110-118.
- 36 [35] S.J. Pennycook, D.E. Jesson, High-resolution Z-contrast imaging of crystals,
- 37 Ultramicroscopy 37(1-4) (1991) 14-38.
- 38 [36] M. Mostafavi, D.M. Collins, B. Cai, R. Bradley, R.C. Atwood, C. Reinhard, X. Jiang, M.
- 39 Galano, P.D. Lee, T.J. Marrow, Yield behavior beneath hardness indentations in ductile metals,
- 40 measured by three-dimensional computed X-ray tomography and digital volume correlation,
- 41 Acta Mater. 82 (2015) 468-482.
- 42 [37] M.C. Troparevsky, J.R. Morris, P.R.C. Kent, A.R. Lupini, G.M. Stocks, Criteria for
- Predicting the Formation of Single-Phase High-Entropy Alloys, Phys. Rev. X 5(1) (2015).

- 1 [38] S. Guo, C.T. Liu, Phase stability in high entropy alloys: Formation of solid-solution
- 2 phase or amorphous phase, Progress in Natural Science: Materials International 21(6) (2011)
- 3 433-446.
- 4 [39] Y. Zhang, Y.J. Zhou, J.P. Lin, G.L. Chen, P.K. Liaw, Solid-Solution Phase Formation
- 5 Rules for Multi-component Alloys, Advanced Engineering Materials 10(6) (2008) 534-538.
- 6 [40] X.Q. Chen, V.T. Witusiewicz, R. Podloucky, P. Rogl, F. Sommer, Computational and
- 7 experimental study of phase stability, cohesive properties, magnetism and electronic structure
- 8 of TiMn2, Acta Mater. 51(5) (2003) 1239-1247.
- 9 [41] S. Guo, C. Ng, J. Lu, C.T. Liu, Effect of valence electron concentration on stability of fcc
- or bcc phase in high entropy alloys, Journal of Applied Physics 109(10) (2011).
- 11 [42] X. Yang, Y. Zhang, Prediction of high-entropy stabilized solid-solution in
- multi-component alloys, Materials Chemistry and Physics 132(2-3) (2012) 233-238.
- 13 [43] X. Yang, S.Y. Chen, J.D. Cotton, Y. Zhang, Phase Stability of Low-Density,
- 14 Multiprincipal Component Alloys Containing Aluminum, Magnesium, and Lithium, Jom
- 15 66(10) (2014) 2009-2020.
- 16 [44] S. Guo, Q. Hu, C. Ng, C.T. Liu, More than entropy in high-entropy alloys: Forming solid
- solutions or amorphous phase, Intermetallics 41 (2013) 96-103.
- 18 [45] A. Jain, S.P. Ong, G. Hautier, W. Chen, W.D. Richards, S. Dacek, S. Cholia, D. Gunter, D.
- 19 Skinner, G. Ceder, K.A. Persson, Commentary: The Materials Project: A materials genome
- approach to accelerating materials innovation, APL Mater. 1(1) (2013).
- 21 [46] S. Kirklin, J.E. Saal, B. Meredig, A. Thompson, J.W. Doak, M. Aykol, S. Rühl, C.
- 22 Wolverton, The Open Quantum Materials Database (OQMD): assessing the accuracy of DFT
- 23 formation energies, npj Comput. Mater. 1(1) (2015).
- 24 [47] L. Vegard, Die Konstitution der Mischkristalle und die Raumfllung der Atome,
- 25 Zeitschrift fr Physik 5(1) (1921) 17-26.
- 26 [48] L. Ma, R.-K. Pan, S.-C. Zhou, T.-P. Luo, D.-H. Wu, T.-W. Fan, B.-Y. Tang, Ab initio
- 27 study of stacking faults and deformation mechanism in C15 Laves phases Cr2X (X = Nb, Zr,
- 28 Hf), Materials Chemistry and Physics 143(2) (2014) 702-706.
- 29 [49] J.-W. Yeh, Physical Metallurgy, High-Entropy Alloys 2016, pp. 51-113.
- 30 [50] D.E. Luzzi, Analysis of stacking faults in the Hf-V-Nb cubic laves phase, Scripta
- 31 Materialia 37(6) (1997) 713-720.
- 32 [51] P.C.J. Gallagher, The influence of alloying, temperature, and related effects on the
- 33 stacking fault energy, Metallurgical and Materials Transactions B 1(9) (1970) 2429–2461.
- 34 [52] S.M. Shaikh, V.S. Hariharan, S.K. Yadav, B.S. Murty, CALPHAD and rule-of-mixtures:
- 35 A comparative study for refractory high entropy alloys, Intermetallics 127 (2020).
- 36 [53] MathWorks, Fit Gaussian Mixture Model to Data.
- 37 https://www.mathworks.com/help/stats/fit-a-gaussian-mixture-model-to-data.html, (2016).
- 38 [54] J.P. Couzinié, L. Lilensten, Y. Champion, G. Dirras, L. Perrière, I. Guillot, On the room
- 39 temperature deformation mechanisms of a TiZrHfNbTa refractory high-entropy alloy,
- 40 Materials Science and Engineering: A 645 (2015) 255-263.
- 41 [55] Y. Zou, S. Maiti, W. Steurer, R. Spolenak, Size-dependent plasticity in an
- 42 Nb25Mo25Ta25W25 refractory high-entropy alloy, Acta Mater. 65 (2014) 85-97.

- 1 [56] J. Wu, L. Wen, B.-Y. Tang, L.-M. Peng, W.-J. Ding, Generalized planner fault energies,
- 2 twinning and ductility of L12 type Al3Sc and Al3Mg, Solid State Sciences 13(1) (2011)
- 3 120-125.
- 4 [57] C. Zehnder, K. Czerwinski, K.D. Molodov, S. Sandlöbes-Haut, J.S.K.L. Gibson, S.
- 5 Korte-Kerzel, Plastic deformation of single crystalline C14 Mg2Ca Laves phase at room
- 6 temperature, Materials Science and Engineering: A 759 (2019) 754-761.
- 7 [58] J.R. Rice, Dislocation nucleation from a crack tip: An analysis based on the Peierls
- 8 concept, Journal of the Mechanics and Physics of Solids 40(2) (1992) 239-271.
- 9 [59] K. Inoue, K. Tachikawa, On the superconducting properties of the
- 10 V<inf&gt;2&lt;/inf&gt;Hf-base laves phase compound tapes, IEEE Transactions on
- 11 Magnetics 13(1) (1977) 840-843.
- 12 [60] F. Chu, D.P. Pope, Deformation twinning in intermetallic compounds—the dilemma of
- shears vs. shuffles, Materials Science and Engineering: A 170(1-2) (1993) 39-47.
- 14 [61] T. Takasugi, M. Yoshida, S. Hanada, Deformability improvement in C15 NbCr2
- intermetallics by addition of ternary elements, Acta Mater. 44(2) (1996) 669-674.
- 16 [62] T. Takasugi, M. Yoshida, S. Hanada, Microstructure and high-temperature deformation of
- the C15 NbCr2-based Laves intermetallics in Nb-Cr-V alloy system, Journal of Materials
- 18 Research 10(10) (2011) 2463-2470.
- 19 [63] Y. Kimura, D.E. Luzzi, D.P. Pope, Deformation twinning in a HfV2+Nb-based laves
- phase alloy, Materials Science and Engineering: A 329-331 (2002) 241-248.
- 21 [64] J.D. Livingston, E.L. Hall, Room-temperature deformation in a Laves phase, Journal of
- 22 Materials Research 5(1) (2011) 5-8.
- 23 [65] J.A. Venables, Deformation twinning in face-centred cubic metals, Philosophical
- 24 Magazine 6(63) (1961) 379-396.